Extracellular Vesicles from *PRPF31*$^{+/-}$ iPSC-Derived RPE Have a Distinct RNA Profile Compared to Those From Healthy RPE

Heran Getachew[1], Sudeep Mehrotra[1], Rosario Fernandez-Godino[1], and Eric A. Pierce[1*]

[1]Ocular Genomics Institute, Department of Ophthalmology, Mass Eye and Ear, Harvard Medical School, Boston, MA

*Address correspondence to:

Eric Pierce

Ocular Genomics Institute

Mass Eye and Ear

243 Charles St.

Boston, MA 02114

Eric_pierce@meei.harvard.edu

Abstract

Retinitis pigmentosa (RP) is the most common form of inherited retinal degeneration (IRD) and causes vision loss via dysfunction and death of the photoreceptor cells and retinal pigment epithelium (RPE) of the retina. Mutations in pre-mRNA processing factor 31 (PRPF31) are associated with autosomal dominant RP, and are thought to cause retinal degeneration by causing cell autonomous defects in RPE function. Genetic therapies such as adeno-associated virus (AAV) mediated gene therapy show great promise for treating IRDs, however in many cases it is challenging to measure clinical efficacy in a timely manner because IRDs progress slowly. A potential solution to this challenge is the use of additional outcome measures, such as biomarkers. Extracellular vesicles (EVs) are lipid enclosed vesicles that are secreted by cells and their RNA contents have been proposed as potential biomarkers in cancer and other diseases. We hypothesize EV RNAs can be used as biomarkers of the health status of the neural retina and RPE. To test this hypothesis for the RPE, we used *PRPF31*$^{+/+}$ and *PRPF31*$^{+/-}$ human induced pluripotent stem cell (hiPSC)-derived RPE to investigate the RNAs contained in RPE-derived EVs, and how they change in disease. We also compared the RNA contents of RPE-EVs with the RNAs contained in the hiPSC-RPE cells themselves. We found that EVs from mutant *PRPF31*$^{+/-}$ hiPSC-RPE cells contain distinct RNAs compared to EV from the control *PRPF31*$^{+/+}$ hiPSC-RPE cells, suggesting EV RNA contents change during disease and can potentially serve as biomarkers of retinal degeneration.

Introduction

Inherited retinal degenerations (IRDs) are important causes of vision loss in both children and adults (1, 2). Rod-cone degeneration, also called retinitis pigmentosa (RP) is the most common form of IRD, and affects approximately 1 in 3500 individuals worldwide (3). IRD and RP pathology includes degeneration of the retinal pigment epithelium (RPE) and neural retina, which leads to vision loss (4). Mutations in pre-RNA processing factors (PRPFs) are among the most common causes of autosomal dominant RP (5, 6). Among the PRPFs, mutations in *PRPF31* are the most common, accounting for approximately 10% of dominant RP (7). Of interest, mutations in *PRPF31* have been shown to cause dominant disease via haploinsufficiency (8).

Mouse models of *PRPF31*-associated RP have shown that haploinsufficiency of PRPF31 causes cell autonomous defects in RPE function, including reduced phagocytosis of photoreceptor outer segments, one of the key functions of the RPE in vision (references). Furthermore, *PRPF31*$^{+/-}$ mutant human induced pluripotent stem cell (hiPSC) derived RPE cells exhibit reduced phagocytosis function, shorter cilia and microvilli, and reduced barrier function of the RPE (9, 10). Adeno-associated virus (AAV) mediated gene augmentation therapy was able to restore normal function to *PRPF31*$^{+/-}$ iPSC-RPE cells, suggesting its potential use to treat *PRPF31*-associated RP (9).

Genetic therapies including AAV – mediated gene therapy has demonstrated great promise for the treatment of IRDs (11-15). Many IRDs advance slowly, and central vision can be retained until late in disease. A challenge in clinical trials of potential treatments of IRDs is demonstrating the benefit of treatment in a timely manner as it can take years for improvement in clinical outcome measures such as visual acuity and visual fields to become detectable (16). For

these reasons, surrogate measures of the health status of the retina would be of great benefit to IRD clinical trials. Cancer clinical trials have used the detection of circulating tumor-derived DNA (ctDNA) and RNA as a measure of disease status, including FDA-approved liquid biopsies to detect ctDNA in plasma for prostate and non-small cell lung cancers (17-19). Circulating tumor-derived DNA is present freely circulating and within extracellular vesicles (EVs). EVs are lipid-enclosed vesicles, ranging in size from less than 50 nm to micrometers in diameter, secreted from virtually all cell types and found in several biofluids including plasma and the vitreous humor of the eye. EVs have been proposed as biomarkers because they contain proteins and nucleic acids from their source cells, leading to the hypothesis that EV contents change during disease and can potentially act as surrogates to assess the health status of their source cells (20-25). Several groups have evaluated the use of RNAs in EVs from the vitreous, aqueous and serum as biomarkers of uveal melanoma, age-related macular degeneration, and glaucoma (26-30). The protein contents of EVs produced by the RPE have also been studied (31, 32).

In order to use EV RNAs as biomarkers for PRPF31-associated RP as well as other IRDs affecting the RPE, the RPE EV transcriptome must be defined, which has not been done to date. In the studies reported here, we define the RNA profiles of EVs produced by control *PRPF31*$^{+/+}$ and mutant *PRPF31*$^{+/-}$ iPSC-RPE. We also compared the RNA contents of RPE-derived EVs with the transcriptomes of the control and mutant hiPSC-RPE cells themselves. Data obtained in these studies support the potential use of RNA biomarkers to assess health status of the RPE.

Results

Characterization of EVs from released from *PRPF31*$^{+/+}$ and *PRPF31*$^{+/-}$ hiPSC-RPE cells

We previously generated hiPSCs with a 10 bp deletion in exon 7 of the *PRPF31* gene. RPE cells differentiated from these mutant *PRPF31*$^{+/-}$ mutant hiPSCs produce reduced levels of PRPF31, and demonstrate defects in phagocytosis function, cilia formation and barrier function compared to RPE from isogenic control hiPSCs (9, 10). To investigate the effects of *PRPF31* haploinsufficiency and RPE dysfunction on the EVs produced by RPE cells, 12 wells each of differentiated *PRPF31*$^{+/+}$ and *PRPF31*$^{+/-}$ iPSC-RPE cells were cultured on transwells for 4 weeks. Then, apical and basal conditioned media was collected for 12 weeks. EVs were isolated from the conditioned media from both control *PRPF31*$^{+/+}$ and mutant *PRPF31*$^{+/-}$ iPSC-RPE cells and analyzed using nanoparticle tracking analysis (NTA) technology to determine the size and concentration. The majority diameters from both *PRPF31*$^{+/+}$ and PRPF31$^{+/-}$ cells ranged from 100-500 nm, with no difference in sizes for *PRPF31*$^{+/+}$ and PRPF31$^{+/-}$ EVs (Figure 1A,B). There was no significant difference in the number of EVs secreted from *PRPF31*$^{+/+}$ and PRPF31$^{+/-}$ cells (Figure 1A,C). EVs were further characterized by transmission electron microscopy and revealed a heterogenous population of cup-shaped EV morphologies in both *PRPF31*$^{+/+}$ and PRPF31$^{+/-}$ derived EVs (Figure 1D).

PRPF31$^{+/+}$ and *PRPF31*$^{+/-}$ EVs have distinct miRNA and Poly-A RNA profiles

To investigate the effects of *PRPF31* haploinsufficiency and RPE dysfunction on the RNA contents of RPE EVs, we sequenced the miRNAs and Poly-A RNAs contained in EVs produced by control *PRPF31*$^{+/+}$ and mutant *PRPF31*$^{+/-}$ hiPSC-RPE. The EVs isolated from the conditioned media of the 12 wells of hiPSC-RPE cells described above were used for these

analyses. Total RNA was prepared from the EVs isolated from the conditioned media of the 12 wells of control *PRPF31*$^{+/+}$ and 12 wells of mutant *PRPF31*$^{+/-}$ hiPSC-RPE. Both miRNA and poly-A RNA (mRNA) libraries were prepared from the EV RNA isolated from each of these 12 experimental and control cultures.

In order to define the profile of miRNAs within iPSC-RPE derived EVs, the 48 EV (24 apical and 24 basal) miRNA libraries were multiplexed to reduced batch effects and sequenced on an Illumina MiSeq instrument. A total of at least 2 million sequence reads were obtained for each miRNA library. Analyses of these data identified a total of 109 miRNAs within hiPSC-RPE EVs (Figure 2A). To determine if there are potential miRNA biomarkers present, we compared the miRNAs contained in *PRPF31*$^{+/+}$ and *PRPF31*$^{+/-}$ iPSC-RPE EVs and found no miRNAs unique to *PRPF31*$^{+/+}$ EVs and 1 unique miRNA, hsa-miR-9-5p, to *PRPF31*$^{+/-}$ EVs (Figure 2A). Furthermore, when we performed differential expression analysis, we found 3 upregulated and 10 downregulated miRNAs in *PRPF31*$^{+/-}$EVs (Figure 2B).

In addition to miRNAs, EVs have been reported to contain poly-adenylated (poly-A) RNAs such as mRNAs as well (20). To define the poly-A contents of EVs produced by the hiPSC-RPE, poly-A RNA libraries were prepared from the 24 EV RNA samples, multiplexed to reduced batch effects and sequenced on an Illumina NovaSeq instrument. At least 200 million sequence reads were obtained for each library to provide good depth of sampling. Analyses of these poly-A RNA-seq data showed that a total of 31,942 poly-A RNAs were identified within the iPSC-RPE EVs. Of the RNA biotypes identified, the majority were protein coding mRNAs (58%) followed by long non-coding RNAs (lncRNAs; 27%). With regard to changes in EV RNA contents in disease, 89 poly-A RNAs were unique to *PRPF31*$^{+/+}$ EVs and 100 poly-A RNAs were unique to *PRPF31*$^{+/-}$ EVs (Figure 3A). A total of 2,176 poly-A RNAs were differentially

expressed, of these, 657 were upregulated and 1,518 downregulated in *PRPF31*$^{+/-}$ EVs (Figure 3B). Gene Set Enrichment Analysis of the differentially expressed genes found enriched cellular components identified in integral component of the plasma membrane, dendrite, and dendritic tree categories in the *PRPF31*$^{+/-}$ EVs. There was no KEGG pathway enrichment detected among the differentially expressed genes. The majority of the uniquely expressed poly-A RNAs present within *PRPF31*$^{+/+}$ and *PRPF31*$^{+/-}$ EVs were pseudogenes and lncRNAs, so there was no Kegg pathway enrichment.

Previous studies have reported that proteins found within EVs reflect the polarity of the RPE (31, 32). In order to determine if RNAs within RPE EVs reflect polarity, we compared all apically and basally released miRNAs and Poly-A RNAs among *PRPF31*$^{+/+}$ and *PRPF31*$^{+/-}$ EVs. We found no miRNAs that were unique to either apical or basal EVs (Figure 4A). Differential expression analysis showed 35 miRNAs were upregulated in apical EVs compared to basal EVs (Figure 4B). There were 144 and 39 poly-A RNAs unique to apical and basal EVs, respectively (Figure 4C). Additionally, there were 9,166 poly-A RNAs enriched in apical EVs and 9,027 enriched in basal EVs (Figure 4D). These data are consistent with the concept that RPE apical and basal EVs exhibit distinct transcriptomes as well as protein contents (31, 32).

<u>The majority of the poly-A RNA profile of EVs is shared with iPSC-RPE cells</u>

To test the hypothesis that EV RNAs can be used as surrogate biomarkers for the health status of their source cells, we performed RNA-seq analyses of poly-A RNAs from the *PRPF31*$^{+/+}$ and *PRPF31*$^{+/-}$iPSC-RPE cells and compared the results to the corresponding poly-A RNA EV data. We found that the majority of poly-A RNAs expressed in hiPSC-RPE cells are contained in the RPE-derived EVs. EVs produced by the control *PRPF31*$^{+/+}$ iPSC-RPE

contained 89% (19,193) of the 21,638 poly-A RNAs identified in the hiPSC-RPE (Figure 5A). Similarly, EVs produced by the mutant *PRPF31*$^{+/-}$ iPSC-RPE contained 89% of the 19,961 poly-A RNAs identified in the mutant hiPSC-RPE (Figure 5B). These results indicate the EVs produced by hiPSC-RPE cells contain the great majority of RNAs of their parent cells, supporting the use of EV RNAs as biomarkers. Interestingly, the EVs produced by the RPE cells also contained many additional poly-A RNAs not identified within their parent cells. *PRPF31*$^{+/+}$ EVs contained 12,178 unique poly-A RNAs and *PRPF31*$^{+/-}$ EVs contained 13,499 unique poly-A RNAs not found within corresponding hiPSC-RPE transcriptomes (Figure 5A,B).

Next, we compared the common poly-A RNAs shared between EVs and iPSC-RPE with the potential biomarkers identified from the poly-A RNAs that were unique or enriched in the EVs produced by the control or mutant hiPSC-RPE cells. These comparisons showed that 975 (61%) of the 1607 potential poly-A RNA biomarkers found in EVs produced by the wild-type *PRPF31*$^{+/+}$ iPSC-RPE cells (89 unique plus 1518 enriched) were present within the 19,193 poly-A RNAs shared between the *PRPF31*$^{+/+}$ EVs and iPSC-RPE cells (Figure 5C). Similarly, 166 (22%) of the 757 potential poly-A RNA biomarkers found in EVs produced by the mutant *PRPF31*$^{+/-}$ iPSC-RPE cells (100 unique plus 657 enriched) were present within the 17,861 poly-A RNAs shared between the *PRPF31*$^{+-+}$ EVs and iPSC-RPE cells (Figure 5B). These results also support the use of EV RNAs as biomarkers of RPE health status and raise intriguing questions about the process of sorting of RNAs from host cells into EVs, as well as the potential functions of RNAs in EVs derived from the RPE (23, 33, 34).

Discussion

The use of EVs biomarkers for disease is a newly emerging field. Here, we report the miRNA and Poly-A RNA profiles of EVs produced by control *PRPF31*$^{+/+}$ and mutant *PRPF31*$^{+/-}$ hiPSC-RPE cells. The RNA profiles of *PRPF31*$^{+/+}$ EVs provide valuable information about the EVs secreted by healthy RPE cells, which can be used as a reference for future work focusing on other RPE disease models, and studies of RPE EV function. By comparing the RNA profiles of *PRPF31*$^{+/+}$ EVs and *PRPF31*$^{+/-}$ EVs we found uniquely and differentially expressed RNAs and in turn, we identified 1607 and 757 potential biomarkers for healthy RPE and *PRPF31*$^{+/-}$ RPE cells, respectively. Our findings support the hypothesis that EV contents change during disease allowing for their potential use as biomarkers.

In assessing the potential use of EV RNAs as biomarkers of RPE health, we compared the poly-A RNA profiles of EVs and their source cells. We found the majority (89%) of the poly-A RNAs detected in the parent RPE cells were contained in the EVs derived from those cells, supporting the concept that EV RNAs reflect the health status of the cells they are derived from (20-25). Of interest, we also found a significant number of poly-A RNAs only detected in EVs. Other studies have reported similar differences in RNA profiles and abundance when comparing EVs to their source cells (35, 36). Although the mechanism of RNA sorting and loading into EVs is currently unknown, some studies suggest the contents of EVs are loaded by source cells as a mechanism of controlling intracellular availability of certain RNAs (23, 33, 34). It is also important to consider for this study and many others, EVs are isolated from pooled conditioned media that is collected for several weeks, while source cell RNA is isolated from one time point, so differences can also be due temporal RNA expression differences at the time of sample collection.

This work focused on primarily on defining EV RNA profiles in order to identify potential biomarkers for healthy RPE and mutant *PRPF31*$^{+/-}$ RPE. These studies can also help inform future studies on the potential of intercellular signaling via EVs in the RPE. It has been previously demonstrated that mRNAs and miRNAs can be transferred via EVs and in turn regulate gene expression of recipient cells (37-41). Flores-Bellver et al performed an experiment where EVs from GFP-expressing RPE cells were incubated to non-GFP RPE cells and upon uptake of the EVs, the recipient cells expressed GFP, indicating that RPE can functionally uptake EVs and their protein contents (32). Future studies are needed to determine if EV RNAs contents can also be transferred from the RPE to other retinal cells and regulate gene expression in the recipient cells. For example, in many ways RPE and photoreceptor cells function together, with coordinated metabolism and RPE cells phagocytosing shed photoreceptor outer segments (42). Since overall retinal function and health depends on these shared processes, it is attractive to hypothesize that EVs may be used for intercellular signaling between the RPE and photoreceptor cells, however further studies are needed to support this hypothesis (43).

We performed this work in an effort to identify potential EV RNA biomarkers of retinal and RPE health, with the ultimate goal of finding biomarkers to use in clinical trials of potential therapies for IRDs, such as AAV-mediated gene therapies (44). For example, we previously demonstrated that AAV-mediated gene therapy restores the function of the RPE in the same *PRPF31*$^{+/-}$ model used in the current work (9). The information obtained from our study can be applied to future applications of *PRPF31* gene therapy as well as other gene therapies directed at treatment of retinal disorders associated with genes expressed in the RPE or associated with RPE dysfunction. In conclusion, we defined the RNA profiles in *PRPF31*$^{+/+}$ and *PRPF31*$^{+/-}$ iPSC-

RPE EVs. In this model, we demonstrated that EV RNA contents change during disease and identified potential EV RNA biomarkers to detect RPE health status.

Materials and Methods

RPE culture and EV isolation

Wildtype *PRPF31*$^{+/+}$ and mutant *PRPF31*$^{+/-}$ hiPSC-RPE cells were previously edited and differentiated (9). hiPSC-RPE cells were seeded onto Matrigel-coated 24-mm polystyrene transwells with 0.4-µm pores (3450, Corning, Bedford, MA, USA) at a density of 700,500 cells per well. The cells were matured for 4 weeks on transwells before conditioned media was collected. Apical and basal conditioned media was collected and stored at -80°C every other day for 14 weeks. The conditioned media was thawed on ice and centrifuged 3000 × g for 15 minutes to remove cells and cell debris. EVs were isolated using ExoQuick-TC (EXOTC50A-1, System Biosciences, Palo Alto, CA, USA) according to manufacturer instructions. Briefly, the conditioned was mixed with Exoquick-TC and incubated at 4°C for at least 12 hours. Then, ExoQuick-TC/conditioned media mixture was at centrifuged at 1500 × g for 30 minutes and the supernatant was discarded. A final spin was performed at 1500 × g for 5 minutes to remove any residual fluid. The EV pellet was resuspended in 100 µL of 1X phosphate-buffered saline (PBS) and stored at -80°C.

NanoSight analysis of EV size and concentration

The size distribution and concentration of EVs was determined using NanoSight NS300. The EVs were diluted 1:100 in PBS, and 1 mL was used for NanoSight analysis. Nanoparticle Tracking Analysis (NTA) software 2.3 was used to track size and diffusion of nanoparticles.

Transmission Electron Microscopy

EV morphologies visualized using transmission electron microscopy (TEM) using previously established protocols (45). Briefly, the EVs were fixed in 2% paraformaldehyde and loaded on

Formvar-carbon coated grids. The grids were incubated in 1% glutaraldehyde and washed. The samples were contrasted using a 4% uranyl-oxalate solution and embedded using 2% methyl cellulose. The samples were then dried and imaged at 100 kV.

miRNA Sequencing

RNA was isolated from the EVs using the Exoquick RNA column purification kit (EQ808A-1, System Biosciences, Palo Alto, CA, USA). Purified RNA was quantified using a Bioanalyzer and the Agilent RNA 6000 Pico kit (5067-1513, Agilent, Santa Clara, CA, USA). miRNA libraries were prepared from the isolated EV RNA and a water control using the TruSeq Small RNA Library Preparation Kit (RS-200-0012, Illumina, San Diego, CA, USA) using the manufacturer instructions with the modification of performing the adaptor ligation in the presence of 15% polyethylene glycol in order to reduce bias by driving the ligation reactions towards completion as determined by the Extracellular RNA Communication Consortium (46). Adapter dimers were removed by gel purification and the purified cDNA libraries were pooled and normalized 2nM. The pooled libraries were then sequenced single-read, 50bp (1 × 50) on an Illumina MiSeq using version 3 reagents at the Ocular Genomic Institute, MEE, Boston, MA (USA).

miRNA Sequencing Analysis

Base quality per sequence cycle was checked with FastQC (https://www.bioinformatics.babraham.ac.uk/projects/fastqc/). An average minimum mean base quality above Q30 (Phred scale) was observed using MultiQC across the read length for all samples (47). The sample replicates were sequenced across four different sequencing runs. Each sequenced run was independently quality checked. The files were merged and quality checked again for any biases. On average 1.5 million reads were observed across all the samples. Samples less then 1 million

reads were dropped. Illumina TruSeq small RNA adapters were scanned on the 5` and 3` ends and trimmed using Cutadapt. Post trimming, minimum length of 17 bp was maintained. The standard miRDeep2 (v2.0.1.2) was used for the analysis (48). Briefly, mapper module (*mapper.pl*) was used for read alignment against the reference human genome (GRCh38). Identification and quantification of each miRNA was performed by the quantifier module (*quantifier.pl*). Precursor and mature miRNAs sequences of human miRBase (miRNA repository) was used as reference sequence. For novel miRNA prediction, mature miRNA of closely related species (Gorilla gorilla, Pongo Pygmaues, Pan troglodytes and Pan Paniscus) were pooled together for alignment and novel miRNA discoveries. Nuclease free water was added to the samples as a control during sequencing. The counts of miRNA identified and reported in the water sample were used to penalize the identified miRNA in other sample replicates. Samples with alignment rate of <1% were removed. The Trimmed Mean of M-values (TMM) from the edgeR package was used for normalized within and across sample replicates. Post normalization, counts per million (CPM) values were to filter and identify "expressed" miRNA across samples replicates. The standard settings in the edgeR package used for differential analysis. Geneset enrichment analysis; Gene Ontology (GO) and pathways (KEGG) was performed using miEAA (http://www.ccb.uni-saarland.de/mieaa_tool/).

EV Poly-A RNA Sequencing

cDNA was prepared from EV RNA using the Single Cell RNA kit SMART-Seq_V4 Ultra Low Input RNA Kit (634890, Takara, Mountain View, CA, USA) according to manufacturer instructions using 1ng input. Next, poly-A libraries were prepared using the SMARTer ThruPLEX DNA-seq Kit (R400675, Takara, Mountain View, CA, USA). Each library was normalized to 1.5 nM, pooled and 1% PhiX was added. Libraries were sequenced for 101 cycles

(2 × 101bp (PE)) using the NovaSeq 6000 (Illumina) at the Ocular Genomic Institute, MEE, Boston, MA (USA).

RPE poly-A RNA Sequencing

RNA was extracted from hiPSC-RPE cells and Spike-in RNA standards, sequins, were used as a reference in all samples (49). Different sets of sequin mixtures were used, one for wildtype *PRPF31*$^{+/+}$ and another set for mutant *PRPF31*$^{+/-}$ samples. Libraries were prepared using the NEBNext Ultra II Directional RNA Library Prep with Sample Purification Beads (E7765S, New England Biolabs, Ipswich, MA, USA), NEBNext Poly(A) mRNA Magnetic Isolation Module (E7490S, New England Biolabs, Ipswich, MA, USA), and NEBNext Multiplex Oligos for Illumina (E6440S, New England Biolabs, Ipswich, MA, USA). Libraries were normalized, pooled, and sequenced as described above.

RNAseq Analysis

Read and sample level QC was performed. Read quality was assessed with FastQC (https://www.bioinformatics.babraham.ac.uk/projects/fastqc/) and MultiQC. An in-house Perl script was used to check and filter out reads with presence of adapter and ambiguous character, 'N'. The Bowtie2 aligner was used to identify ribosomal contamination (50). Reads aligned to rRNA reference sequences were dropped from all downstream analysis using SAMtools (51). The STAR aligner was used to align PE reads to a mouse reference in two-pass mode within the sample and across replicates for each sample set (52). featureCounts from the Subread package, was used to generate gene expression matrix with the following non-default settings: reads must be paired, both the pairs must be mapped, use only uniquely mapped reads, multi-mapped reads are not counted, chimeric reads were not counted and strand specificity turned on (53). Anaquin was used to further evaluate alignment sensitivity and gene expression (54). Here sensitivity

indicates the fraction of annotated regions covered by alignment. The Picard tools (http://broadinstitute.github.io/picard/) and RSeQC were used to calculate mean fragment length (55). The approach implemented in Kallisto was used to covert raw reads to TPM values (56). An average TPM of the lowest Sequins between test and control samples was calculated and used as cutoff. DESeq2 was used for differential gene expression analysis (57). RNA-seq analysis is described in detail in Mehrotra et al. (58). g:Profiler (Ref, version e101_eg48_p14_baf17f0) with a custom background gene set was used for gene set enrichment analysis (GSEA), pathway enrichment and transcription factor binding site analysis (59).

Acknowledgements

The research reported was supported by a Stein Innovation Award from Research to Prevent Blindness (EAP), and a grant from the National Eye Institute (RO1 EY020902, EAP). We are grateful for the contributions of other Ocular Genomics Institute team members, including Daniela Pignatta and the Ocular Genomics Core for their assistance with the RNA-seq. We also acknowledge Philip Seifert and the Schepens Eye Research Institute Morphology Core for their assistance with the TEM imaging. We thank Amanda Fernández-Rodríguez for her assistance with miRNA sequencing analysis.

References

1. Sahel JA, Marazova K, Audo I. Clinical characteristics and current therapies for inherited retinal degenerations. Cold Spring Harb Perspect Med. 2014;5(2):a017111.

2. Schneider N, Sundaresan Y, Gopalakrishnan P, Beryozkin A, Hanany M, Levanon EY, et al. Inherited retinal diseases: Linking genes, disease-causing variants, and relevant therapeutic modalities. Prog Retin Eye Res. 2021:101029.

3. Nishiguchi KM, Rivolta C. Genes associated with retinitis pigmentosa and allied diseases are frequently mutated in the general population. PloS one. 2012;7(7):e41902.

4. Berson EL. Retinitis pigmentosa. The Friedenwald Lecture. Invest Ophthalmol Vis Sci. 1993;34(5):1659-76.

5. Vithana EN, Abu-Safieh L, Allen MJ, Carey A, Papaioannou M, Chakarova C, et al. A human homolog of yeast pre-mRNA splicing gene, PRP31, underlies autosomal dominant retinitis pigmentosa on chromosome 19q13.4 (RP11). Molecular cell. 2001;8(2):375-81.

6. Tanackovic G, Ransijn A, Thibault P, Abou Elela S, Klinck R, Berson EL, et al. PRPF mutations are associated with generalized defects in spliceosome formation and pre-mRNA splicing in patients with retinitis pigmentosa. Hum Mol Genet. 2011;20(11):2116-30.

7. Daiger SP, Sullivan LS, Bowne SJ. Genes and mutations causing retinitis pigmentosa. Clin Genet. 2013;84(2):132-41.

8. Ruberto FP, Balzano S, Namburi P, Kimchi A, Pescini-Gobert R, Obolensky A, et al. Heterozygous deletions of noncoding parts of the PRPF31 gene cause retinitis pigmentosa via reduced gene expression. Mol Vis. 2021;27:107-16.

9. Brydon EM, Bronstein R, Buskin A, Lako M, Pierce EA, Fernandez-Godino R. AAV-Mediated Gene Augmentation Therapy Restores Critical Functions in Mutant PRPF31 iPSC-Derived RPE Cells. Molecular Therapy - Methods & Clinical Development. 2019;15:392-402.

10. Buskin A, Zhu L, Chichagova V, Basu B, Mozaffari-Jovin S, Dolan D, et al. Disrupted alternative splicing for genes implicated in splicing and ciliogenesis causes PRPF31 retinitis pigmentosa. Nat Commun. 2018;9(1):4234.

11. Banin E, Gootwine E, Obolensky A, Ezra-Elia R, Ejzenberg A, Zelinger L, et al. Gene Augmentation Therapy Restores Retinal Function and Visual Behavior in a Sheep Model of CNGA3 Achromatopsia. Mol Ther. 2015;23(9):1423-33.

12. Komáromy AM, Alexander JJ, Rowlan JS, Garcia MM, Chiodo VA, Kaya A, et al. Gene therapy rescues cone function in congenital achromatopsia. Hum Mol Genet. 2010;19(13):2581-93.

13. Maguire AM, Simonelli F, Pierce EA, Pugh EN, Jr., Mingozzi F, Bennicelli J, et al. Safety and efficacy of gene transfer for Leber's congenital amaurosis. The New England journal of medicine. 2008;358(21):2240-8.

14. Bainbridge JW, Smith AJ, Barker SS, Robbie S, Henderson R, Balaggan K, et al. Effect of gene therapy on visual function in Leber's congenital amaurosis. The New England journal of medicine. 2008;358(21):2231-9.

15. Rodrigues GA, Shalaev E, Karami TK, Cunningham J, Slater NKH, Rivers HM. Pharmaceutical Development of AAV-Based Gene Therapy Products for the Eye. Pharm Res. 2018;36(2):29.

16. Calzetti G, Levy RA, Cideciyan AV, Garafalo AV, Roman AJ, Sumaroka A, et al. Efficacy Outcome Measures for Clinical Trials of USH2A Caused by the Common c.2299delG Mutation. Am J Ophthalmol. 2018;193:114-29.

17. Peng Y, Mei W, Ma K, Zeng C. Circulating Tumor DNA and Minimal Residual Disease (MRD) in Solid Tumors: Current Horizons and Future Perspectives. Frontiers in Oncology. 2021;11.

18. González-Billalabeitia E, Conteduca V, Wetterskog D, Jayaram A, Attard G. Circulating tumor DNA in advanced prostate cancer: transitioning from discovery to a clinically implemented test. Prostate Cancer Prostatic Dis. 2019;22(2):195-205.

19. Yu M, Zhu Y, Teng L, Cui J, Su Y. Can Circulating Cell-Free DNA or Circulating Tumor DNA Be a Promising Marker in Ovarian Cancer? J Oncol. 2021;2021:6627241.

20. Keerthikumar S, Chisanga D, Ariyaratne D, Al Saffar H, Anand S, Zhao K, et al. ExoCarta: A Web-Based Compendium of Exosomal Cargo. J Mol Biol. 2016;428(4):688-92.

21. Ni H, Capodici J, Cannon G, Communi D, Boeynaems JM, Karikó K, et al. Extracellular mRNA induces dendritic cell activation by stimulating tumor necrosis factor-alpha secretion and signaling through a nucleotide receptor. J Biol Chem. 2002;277(15):12689-96.

22. Hoy AM, Buck AH. Extracellular small RNAs: what, where, why? Biochem Soc Trans. 2012;40(4):886-90.

23. Kobayashi M, Salomon C, Tapia J, Illanes SE, Mitchell MD, Rice GE. Ovarian cancer cell invasiveness is associated with discordant exosomal sequestration of Let-7 miRNA and miR-200. J Transl Med. 2014;12:4.

24. La Marca V, Fierabracci A. Insights into the Diagnostic Potential of Extracellular Vesicles and Their miRNA Signature from Liquid Biopsy as Early Biomarkers of Diabetic Micro/Macrovascular Complications. Int J Mol Sci. 2017;18(9).

25. Klingeborn M, Dismuke WM, Bowes Rickman C, Stamer WD. Roles of exosomes in the normal and diseased eye. Prog Retin Eye Res. 2017;59:158-77.

26. Ragusa M, Barbagallo C, Statello L, Caltabiano R, Russo A, Puzzo L, et al. miRNA profiling in vitreous humor, vitreal exosomes and serum from uveal melanoma patients: Pathological and diagnostic implications. Cancer Biol Ther. 2015;16(9):1387-96.

27. Ragusa M, Caltabiano R, Russo A, Puzzo L, Avitabile T, Longo A, et al. MicroRNAs in vitreus humor from patients with ocular diseases. Mol Vis. 2013;19:430-40.

28. ElShelmani H, Wride MA, Saad T, Rani S, Kelly DJ, Keegan D. Identification of Novel Serum MicroRNAs in Age-Related Macular Degeneration. Translational Vision Science & Technology. 2020;9(4):28-.

29. Ertekin S, Yıldırım O, Dinç E, Ayaz L, Fidancı SB, Tamer L. Evaluation of circulating miRNAs in wet age-related macular degeneration. Mol Vis. 2014;20:1057-66.

30. Tanaka Y, Tsuda S, Kunikata H, Sato J, Kokubun T, Yasuda M, et al. Profiles of extracellular miRNAs in the aqueous humor of glaucoma patients assessed with a microarray system. Scientific reports. 2014;4:5089-.

31. Klingeborn M, Dismuke WM, Skiba NP, Kelly U, Stamer WD, Bowes Rickman C. Directional Exosome Proteomes Reflect Polarity-Specific Functions in Retinal Pigmented Epithelium Monolayers. Sci Rep. 2017;7(1):4901.

32. Flores-Bellver M, Mighty J, Aparicio-Domingo S, Li KV, Shi C, Zhou J, et al. Extracellular vesicles released by human retinal pigment epithelium mediate increased polarised secretion of drusen proteins in response to AMD stressors. Journal of Extracellular Vesicles. 2021;10(13):e12165.

33. de Candia P, Torri A, Gorletta T, Fedeli M, Bulgheroni E, Cheroni C, et al. Intracellular modulation, extracellular disposal and serum increase of MiR-150 mark lymphocyte activation. PloS one. 2013;8(9):e75348.

34. Rashed MH, Kanlikilicer P, Rodriguez-Aguayo C, Pichler M, Bayraktar R, Bayraktar E, et al. Exosomal miR-940 maintains SRC-mediated oncogenic activity in cancer cells: a possible role for exosomal disposal of tumor suppressor miRNAs. Oncotarget. 2017;8(12):20145-64.

35. Jovičić A, Gitler AD. Distinct repertoires of microRNAs present in mouse astrocytes compared to astrocyte-secreted exosomes. PloS one. 2017;12(2):e0171418.

36. Otake K, Adachi-Tominari K, Nagai H, Saito M, Sano O, Hirozane Y, et al. Quantitative comparison of the mRNA content of human iPSC-derived motor neurons and their extracellular vesicles. FEBS open bio. 2021;11(2):494-506.

37. Valadi H, Ekstrom K, Bossios A, Sjostrand M, Lee JJ, Lotvall JO. Exosome-mediated transfer of mRNAs and microRNAs is a novel mechanism of genetic exchange between cells. Nat Cell Biol. 2007;9(6):654-9.

38. Montecalvo A, Larregina AT, Shufesky WJ, Stolz DB, Sullivan ML, Karlsson JM, et al. Mechanism of transfer of functional microRNAs between mouse dendritic cells via exosomes. Blood. 2012;119(3):756-66.

39. Zhou J, Flores-Bellver M, Pan J, Benito-Martin A, Shi C, Onwumere O, et al. Human retinal organoids release extracellular vesicles that regulate gene expression in target human retinal progenitor cells. Scientific Reports. 2021;11(1):21128.

40. Zhang Y, Liu D, Chen X, Li J, Li L, Bian Z, et al. Secreted monocytic miR-150 enhances targeted endothelial cell migration. Molecular cell. 2010;39(1):133-44.

41. Pegtel DM, Cosmopoulos K, Thorley-Lawson DA, van Eijndhoven MA, Hopmans ES, Lindenberg JL, et al. Functional delivery of viral miRNAs via exosomes. Proceedings of the National Academy of Sciences of the United States of America. 2010;107(14):6328-33.

42. Hurley JB. Retina Metabolism and Metabolism in the Pigmented Epithelium: A Busy Intersection. Annu Rev Vis Sci. 2021;7:665-92.

43. Strauss O. The retinal pigment epithelium in visual function. Physiol Rev. 2005;85(3):845-81.

44. Botto C, Rucli M, Tekinsoy MD, Pulman J, Sahel JA, Dalkara D. Early and late stage gene therapy interventions for inherited retinal degenerations. Prog Retin Eye Res. 2022;86:100975.

45. Théry C, Amigorena S, Raposo G, Clayton A. Isolation and characterization of exosomes from cell culture supernatants and biological fluids. Curr Protoc Cell Biol. 2006;Chapter 3:Unit 3.22.

46. Giraldez MD, Spengler RM, Etheridge A, Godoy PM, Barczak AJ, Srinivasan S, et al. Comprehensive multi-center assessment of small RNA-seq methods for quantitative miRNA profiling. Nat Biotechnol. 2018;36(8):746-57.

47. Ewels P, Magnusson M, Lundin S, Käller M. MultiQC: summarize analysis results for multiple tools and samples in a single report. Bioinformatics. 2016;32(19):3047-8.

48. Friedländer MR, Mackowiak SD, Li N, Chen W, Rajewsky N. miRDeep2 accurately identifies known and hundreds of novel microRNA genes in seven animal clades. Nucleic Acids Res. 2012;40(1):37-52.

49. Hardwick SA, Chen WY, Wong T, Deveson IW, Blackburn J, Andersen SB, et al. Spliced synthetic genes as internal controls in RNA sequencing experiments. Nat Methods. 2016;13(9):792-8.

50. Langmead B, Salzberg SL. Fast gapped-read alignment with Bowtie 2. Nature Methods. 2012;9(4):357-9.

51. Li H, Handsaker B, Wysoker A, Fennell T, Ruan J, Homer N, et al. The Sequence Alignment/Map format and SAMtools. Bioinformatics. 2009;25(16):2078-9.

52. Dobin A, Davis CA, Schlesinger F, Drenkow J, Zaleski C, Jha S, et al. STAR: ultrafast universal RNA-seq aligner. Bioinformatics. 2012;29(1):15-21.

53. Liao Y, Smyth GK, Shi W. featureCounts: an efficient general purpose program for assigning sequence reads to genomic features. Bioinformatics. 2014;30(7):923-30.

54. Wong T, Deveson IW, Hardwick SA, Mercer TR. ANAQUIN: a software toolkit for the analysis of spike-in controls for next generation sequencing. Bioinformatics. 2017;33(11):1723-4.

55. Wang L, Wang S, Li W. RSeQC: quality control of RNA-seq experiments. Bioinformatics. 2012;28(16):2184-5.

56. Bray NL, Pimentel H, Melsted P, Pachter L. Near-optimal probabilistic RNA-seq quantification. Nat Biotechnol. 2016;34(5):525-7.

57. Love MI, Huber W, Anders S. Moderated estimation of fold change and dispersion for RNA-seq data with DESeq2. Genome Biology. 2014;15(12):550.

58. Mehrotra S, Bronstein R, Navarro-Gomez D, Segrè AV, Pierce EA. Evaluating Methods for Differential Gene Expression And Alternative Splicing Using Internal Synthetic Controls. bioRxiv. 2020:2020.08.05.238295.

59. Raudvere U, Kolberg L, Kuzmin I, Arak T, Adler P, Peterson H, et al. g:Profiler: a web server for functional enrichment analysis and conversions of gene lists (2019 update). Nucleic Acids Research. 2019;47(W1):W191-W8.

Figure Legends

Figure 1. Characterization of EVs from *PRPF31*$^{+/+}$ and PRPF31$^{+/-}$ iPSC-RPE cells. A) Size and concentration distribution of *PRPF31*$^{+/+}$ and *PRPF31*$^{+/-}$ EVs by nanoparticle tracking analysis technology. B) Average size of *PRPF31*$^{+/+}$ EVs was 247.05 ± 16.41 nm and *PRPF31*$^{+/-}$ EVs 206.40 ± 26.35 nm. C) The concentration of *PRPF31*$^{+/+}$ EVs was $3.79 \times 10^9 \pm 1.19 \times 10^9$ EVs/ml and *PRPF31*$^{+/-}$ EVs was $2.67 \times 10^9 \pm 1.12 \times 10^9$ EVs/ml. N=4, error bars: standard error of the mean. D) Transmission electron microscopy images of *PRPF31*$^{+/+}$ and *PRPF31*$^{+/-}$ EVs; scale bar is 100μm.

Figure 2. Comparison of miRNAs from *PRPF31*$^{+/+}$ and PRPF31$^{+/-}$ EVs. A) Venn diagram shows the number of expressed miRNAs above 1 CPM in *PRPF31*$^{+/+}$ and PRPF31$^{+/-}$ EVs. B) Volcano plots show the log2 (fold change) on the x-axis and the -log10(adjusted P-value) on the y-axis.

Figure 3. Comparison of Poly-As from *PRPF31*$^{+/+}$ and PRPF31$^{+/-}$ EVs. A) The Venn diagram shows the number of expressed Poly-As above 1 TPM in *PRPF31*$^{+/+}$ and PRPF31$^{+/-}$ EVs. B) Volcano plots show the log2(fold change) on the x-axis and the -log10(adjusted P-value) on the y-axis.

Figure 4. Comparison of apical and basal EV miRNAs and Poly-As. A,C) Venn diagrams show the number of expressed (A) miRNAs and (C) Poly-As in all apical and basal EVs. B,D) Volcano plots show the log2(fold change) on the x-axis and the -log10(adjusted P-value) on the y-axis.

Figure 5. EV RNA profiles compared to iPSC-RPE source cells. A,B) Venn diagrams represent unique and shared expressed EV Poly-As among (A) *PRPF31*$^{+/+}$ and (B) PRPF31$^{+/-}$ iPSC-RPE cells. C,D) Venn diagrams shows unique and shared Poly-As among iPSC-RPE cells and (top) uniquely expressed (Figure 3A) and (bottom) differentially expressed (Figure 3B) EV Poly-As from (C) *PRPF31*$^{+/+}$ and (D) PRPF31$^{+/-}$ EVs.

Figure 1

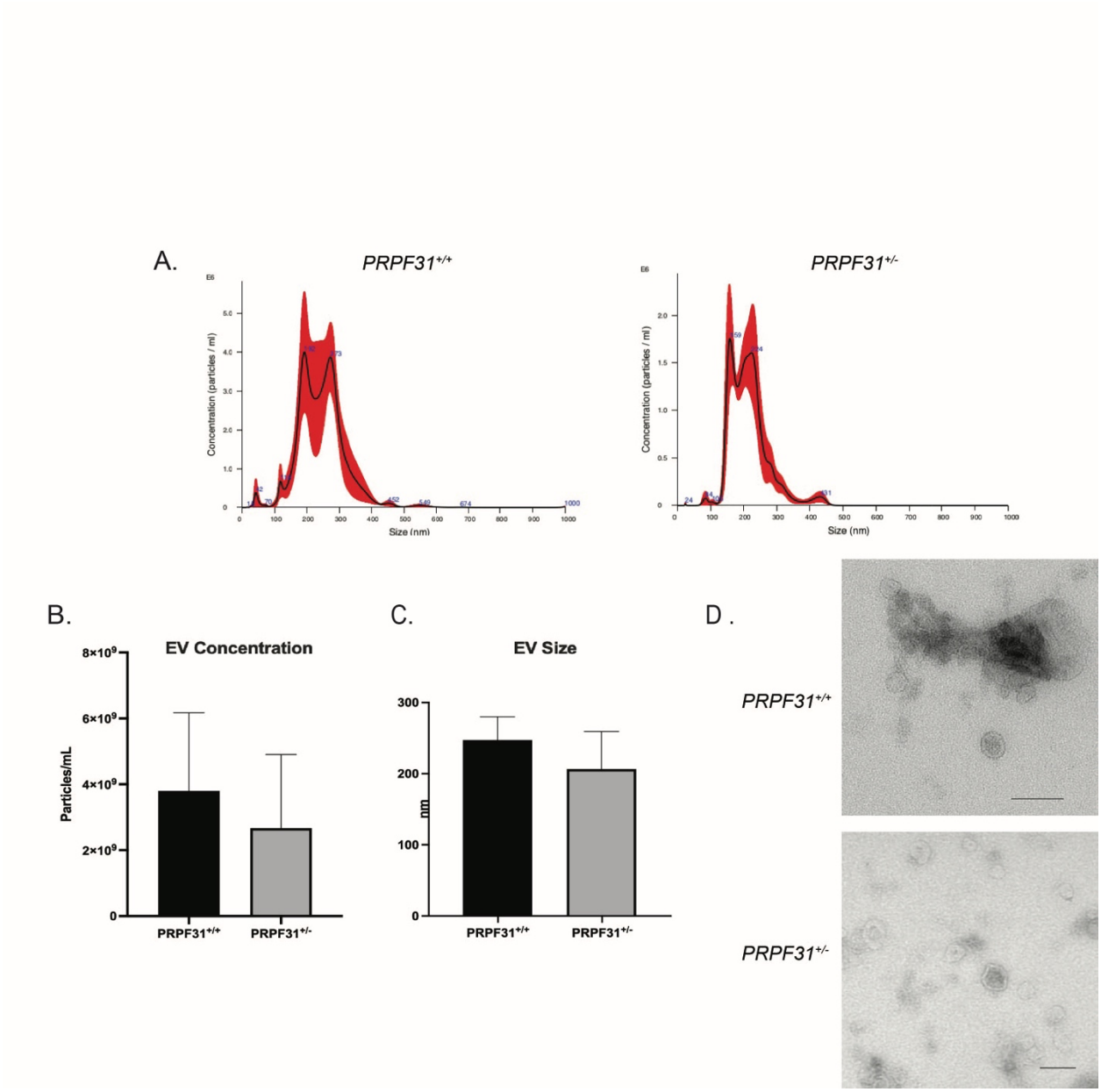
A.
PRPF31+/+
PRPF31+/-
Concentration (particles / ml)
Size (nm)
B.
EV Concentration
Particles/mL
8×10⁹
6×10⁹
4×10⁹
2×10⁹
0
PRPF31+/+
PRPF31+/-
C.
EV Size
nm
300
200
100
0
PRPF31+/+
PRPF31+/-
D .
PRPF31+/+
PRPF31+/-

Figure 2

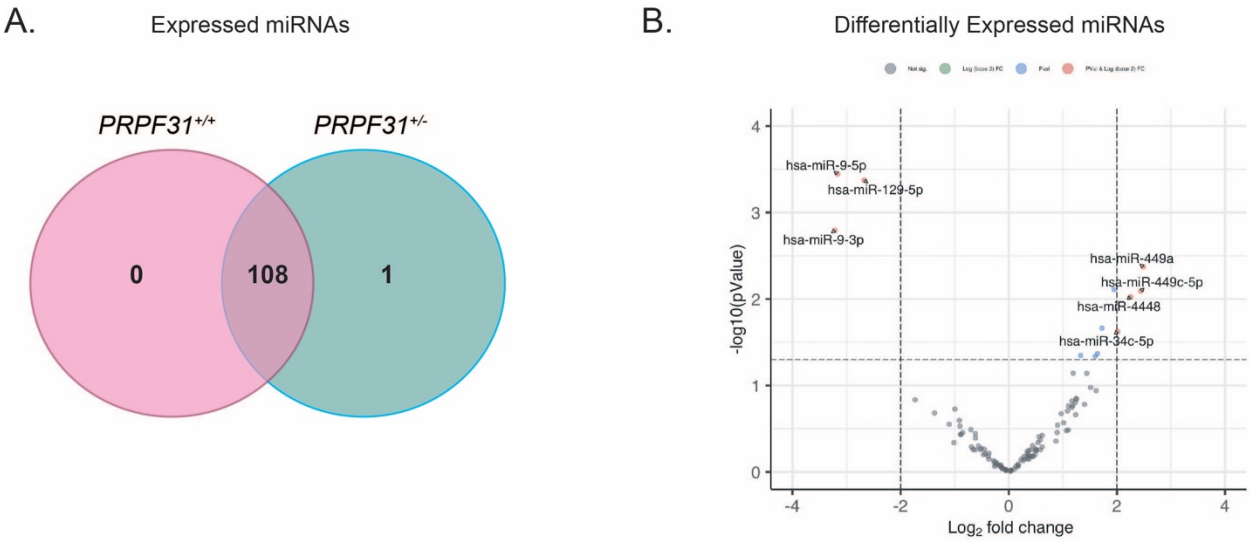

Figure 3

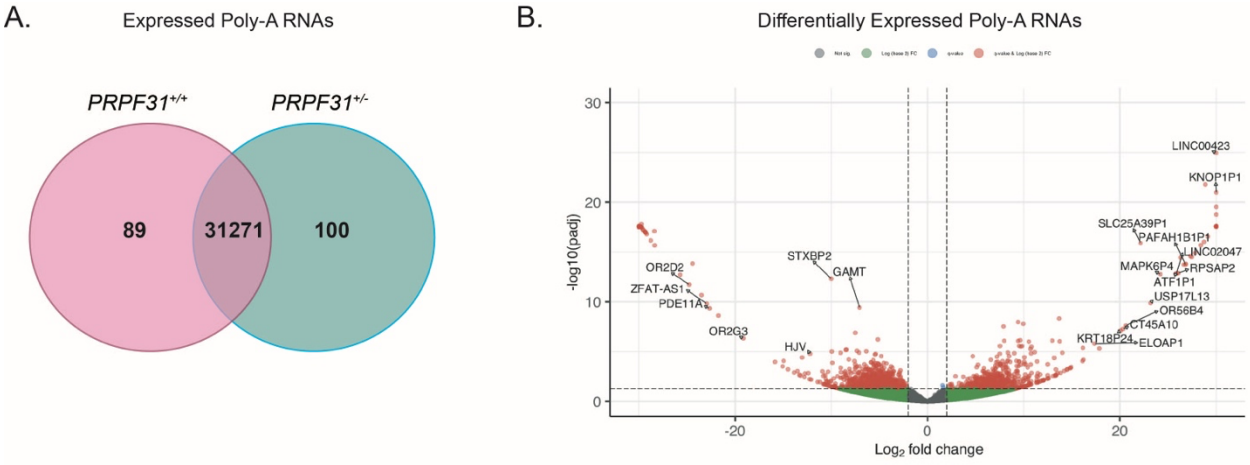

Figure 4

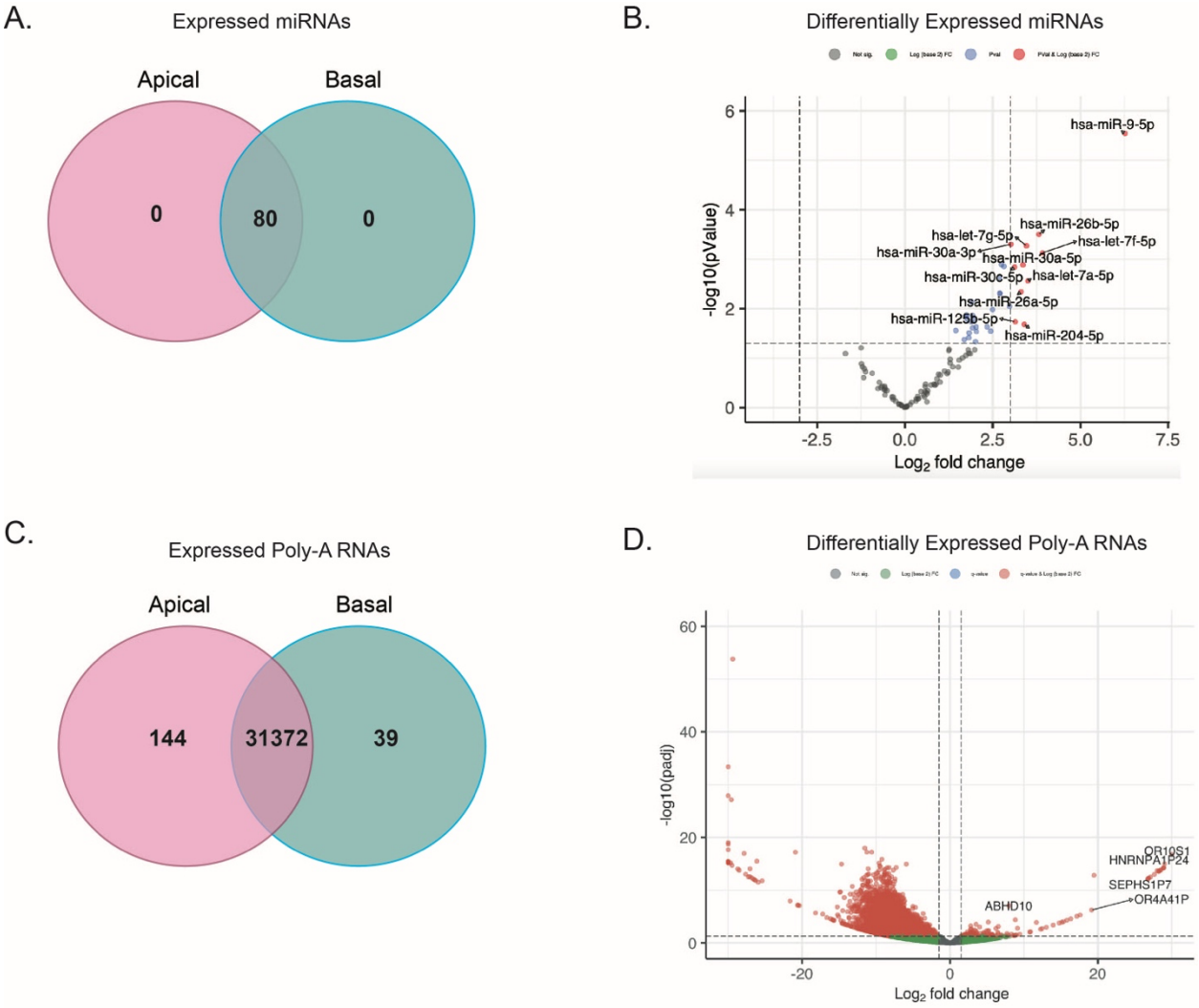
A.
Expressed miRNAs
Apical
Basal
0
80
0
B.
Differentially Expressed miRNAs
hsa-miR-9-5p
hsa-miR-26b-5p
hsa-let-7g-5p
hsa-let-7f-5p
hsa-miR-30a-3p
hsa-miR-30a-5p
hsa-miR-30c-5p
hsa-let-7a-5p
hsa-miR-26a-5p
hsa-miR-125b-5p
hsa-miR-204-5p
-log10(pValue)
Log2 fold change
C.
Expressed Poly-A RNAs
Apical
Basal
144
31372
39
D.
Differentially Expressed Poly-A RNAs
OR10S1
HNRNPA1P24
SEPHS1P7
OR4A41P
ABHD10
-log10(padj)
Log2 fold change

Figure 5

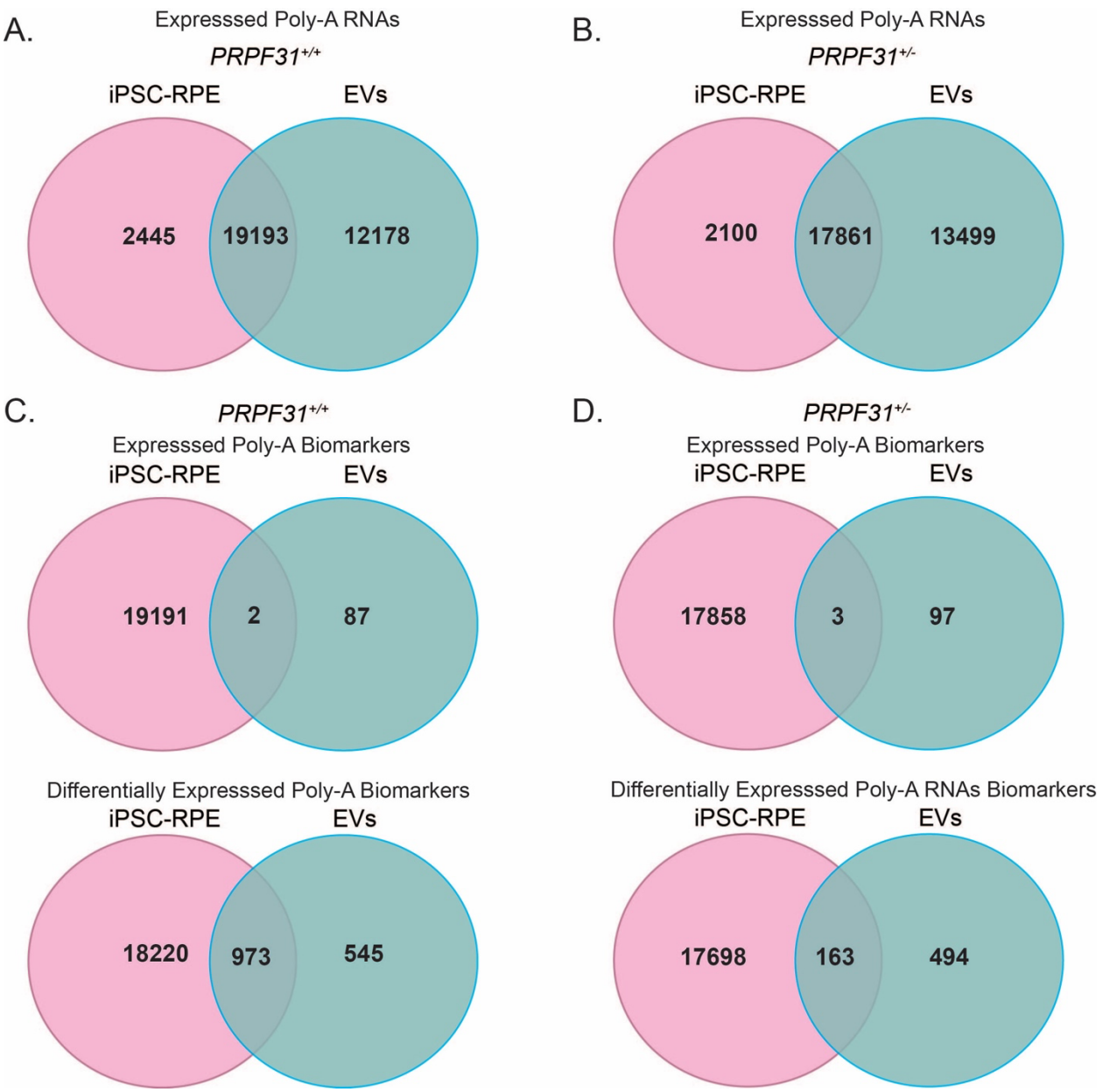
A.
Expresssed Poly-A RNAs
PRPF31+/+
iPSC-RPE
EVs
2445
19193
12178
B.
Expresssed Poly-A RNAs
PRPF31+/-
iPSC-RPE
EVs
2100
17861
13499
C.
PRPF31+/+
Expresssed Poly-A Biomarkers
iPSC-RPE
EVs
19191
2
87
D.
PRPF31+/-
Expresssed Poly-A Biomarkers
iPSC-RPE
EVs
17858
3
97
Differentially Expresssed Poly-A Biomarkers
iPSC-RPE
EVs
18220
973
545
Differentially Expresssed Poly-A RNAs Biomarkers
iPSC-RPE
EVs
17698
163
494